Monthly Notices of the ROYAL ASTRONOMICAL SOCIETY

MNRAS **459,** 2992–3004 (2016) doi:10.1093/mnras/stw806
Advance Access publication 2016 April 12

Spatially resolved integral field spectroscopy of the ionized gas in IZw18★

C. Kehrig,[1]† J. M. Vílchez,[1]† E. Pérez-Montero,[1] J. Iglesias-Páramo,[1,2] J. D. Hernández-Fernández,[3] S. Duarte Puertas,[1] J. Brinchmann,[4,5] F. Durret[6] and D. Kunth[6]

[1]*Instituto de Astrofísica de Andalucía, CSIC, Apartado de correos 3004, E-18080 Granada, Spain*
[2]*Estación Experimental de Zonas Aridas (CSIC), Ctra. de Sacramento s/n, La Caada, Almería, Spain*
[3]*Departamento de Astronomia, Instituto de Astronomia,Geofísica e Ciências Atmosféricas da Universidade de São Paulo, Rua do Matão 1226, Cidade Universitária 05508-090 São Paulo, Brazil*
[4]*Leiden Observatory, Leiden University, PO Box 9513, NL-2300 RA Leiden, the Netherlands*
[5]*Instituto de Astrofísica e Ciências do Espaço, Universidade do Porto, CAUP, Rua das Estrelas, P-4150-762 Porto, Portugal*
[6]*Institut d'Astrophysique de Paris, UMR 7095 CNRS, Université Pierre & Marie Curie, 98 bis boulevard Arago, F-75014 Paris, France*

Accepted 2016 April 5. Received 2016 April 5; in original form 2016 January 25

ABSTRACT

We present a detailed 2D study of the ionized ionized interstellar medium (ISM) of IZw18 using new Potsdam Multi-Aperture Spectrophotometer-integral field unit (PMAS-IFU) optical observations. IZw18 is a high-ionization galaxy which is among the most metal-poor starbursts in the local Universe. This makes IZw18 a local benchmark for understanding the properties most closely resembling those prevailing at distant starbursts. Our IFU aperture ($\sim$1.4 $\times$ 1.4 kpc^2) samples the entire IZw18 main body and an extended region of its ionized gas. Maps of relevant emission lines and emission line ratios show that higher-excitation gas is preferentially located close to the north-west knot and thereabouts. We detect a Wolf–Rayet feature near the north-west knot. We derive spatially resolved and integrated physical–chemical properties for the ionized gas in IZw18. We find no dependence between the metallicity indicator R_{23} and the ionization parameter (as traced by [O III]/[O II]) across IZw18. Over $\sim$0.30 kpc^2, using the [O III] λ4363 line, we compute T_e[O III] values ($\sim$15 000–25 000 K), and oxygen abundances are derived from the direct determinations of T_e[O III]. More than 70 per cent of the higher-T_e[O III] ($\gtrsim$22 000 K) spaxels are He IIλ4686-emitting spaxels too. From a statistical analysis, we study the presence of variations in the ISM physical–chemical properties. A galaxy-wide homogeneity, across hundreds of parsecs, is seen in O/H. Based on spaxel-by-spaxel measurements, the error-weighted mean of $12 + \log(\mathrm{O/H}) = 7.11 \pm 0.01$ is taken as the representative O/H for IZw18. Aperture effects on the derivation of O/H are discussed. Using our IFU data we obtain, for the first time, the IZw18 integrated spectrum.

Key words: H II regions – galaxies: dwarf – galaxies: individual: IZw18 – galaxies: ISM – galaxies: starburst.

1 INTRODUCTION

H II galaxies typically have low masses and blue optical colours, and are the most metal deficient starbursts (sites with intense massive star formation) in the local Universe (e.g. Hunter & Hoffman 1999; Kunth & Östlin 2000; Westera et al. 2004; Kehrig et al. 2006; Izotov, Thuan & Guseva 2012). The optical spectra of H II galaxies are dominated by strong nebular emission lines formed via the ionization of the gas caused by hot massive stars (e.g. Kehrig, Telles & Cuisinier 2004; Cairós et al. 2009a, 2010; Pérez-Montero et al. 2010; Vaduvescu et al. 2014). The cosmological relevance of local metal-poor starburst galaxies has been underscored by the existence of high-redshift starbursts and of the expected primitive galaxies (e.g. Heckman et al. 1998; Schaerer 2003). The latter are supposed to host massive Population III stars (PopIII-stars). Such stars are believed to be the first generation of stars in the Universe and their energetic UV-light could have contributed to the reionization of the Universe (e.g. Tumlinson & Shull 2000; Bromm

★ Based on observations collected at the Centro Astronómico Hispano Alemán (CAHA) at Calar Alto, operated jointly by the Max-Planck-Institut für Astronomie and the Instituto de Astrofísica de Andalucía (CSIC).
† E-mail: kehrig@iaa.es (CK); jvm@iaa.es (JMV)

2013). Investigating low-metallicity H II galaxies in the local Universe can therefore impact our understanding of distant galaxies and galaxy evolution.

The nearby H II galaxy IZw18 is one of the best analogues of primeval galaxies accessible to detailed study (e.g. Papaderos & Östlin 2012; Lebouteiller et al. 2013). This galaxy keeps attracting attention since its discovery (Zwicky 1966) mainly because of its extremely low metallicity (Z ∼1/40 solar metallicity;[1] e.g. Searle & Sargent 1972; Kunth & Sargent 1986; Pagel et al. 1992; Vílchez & Iglesias-Páramo 1998; Izotov & Thuan 1999). IZw18 also shows very blue colours and is rather dust deficient (e.g. van Zee et al. 1998; Fisher et al. 2014). Optical CCD images of IZw18 have revealed a very complex structure with the presence of shells, loops and filaments of ionized gas illustrating the effects of powerful stellar winds in the IZw18's main body and towards its extended gaseous halo (e.g. Davidson, Kinman & Friedman 1989; Hunter & Thronson 1995; Cannon et al. 2002). Several studies of the ionized interstellar medium (ISM) in IZw18 have already been performed, though, despite the complex morphology of the ISM, all these works are mostly based on single-aperture/long-slit spectroscopy of the central star-forming (SF) knots of IZw18 (e.g. Lequeux et al. 1979; Skillman & Kennicutt 1993; Garnett et al. 1997; Izotov & Thuan 1999; Thuan & Izotov 2005; O'Halloran, Madden & Abel 2008).

The importance of integral field spectroscopy (IFS), in comparison to single-aperture/long-slit spectroscopy, for improving our understanding of the warm ISM conditions in different systems has been demonstrated in the literature (e.g. Kehrig et al. 2008; Cairós et al. 2009b; James, Tsamis & Barlow 2010; Monreal-Ibero et al. 2011; Pérez-Montero et al. 2013; Papaderos et al. 2013). A detailed bidimensional spectroscopic study of IZw18, because of its extremely low metal content and high-ionization gas, is relevant to shed light on the ISM properties from galaxies in the intermediate/high-z Universe. In Kehrig et al. (2015), we derive the total HeII-ionizing photon flux in IZw18 and find that peculiar very hot stars, similar to PopIII-stars, are needed to explain the observed nebular HeII emission. As far as we know, here we present the first study based on IFS to investigate the spatially resolved physical–chemical properties (e.g. electron temperature, gaseous metal abundances, excitation) and the spatial correlations that may hold for the warm ISM in IZw18. Our integral field unit (IFU) data reveal the spatially resolved ionization structure for the ionized gas of IZw18, which provide useful boundary conditions for photoionization models at the lowest metallicity regime (e.g. Melekh et al. 2015). Moreover, taking advantage of the IFU data, we derive the integrated physical–chemical characteristics for selected regions, including the IZw18 integrated spectrum, that can be helpful to interpret high-z emission line galaxies. We also discuss the significance of the observed spatial variations of electron temperatures and the oxygen abundance in terms of the observed spatially resolved ionization structure. This can impose constraints on the models for metal dispersal and mixing in H II galaxies, and on the chemical evolution models for conditions close to the ones that prevailed in the primordial Universe (e.g. Recchi et al. 2004; Yin, Matteucci & Vladilo 2011; Recchi & Hensler 2013).

General properties of IZw18 are presented in Table 1. In Fig. 1, we show a three-colour composite image of IZw18 from the *Hubble Space Telescope*/WFPC2 (Baggett et al. 2002). In this image we can see the two main SF regions of IZw18, usually referred to as the north-west (NW) and southeast (SE) components; they are separated by an angular distance of ∼6 arcsec, and dominate in brightness.

[1] Solar metallicity $Z_{\odot} = 0.0134$ (Asplund et al. 2009).

Table 1. General properties of IZw18.

Parameter	IZw18
Other designation	Mrk 116, UGCA 166
Morphological type[a]	i0-type BCD
R.A. (J2000.0)	$09^{h}34^{m}02\overset{s}{.}0$
Dec. (J2000.0)	$+55^{\circ}14'28''$
Redshift	0.0025
D[b](Mpc)	18.2
Scale (pc arcsec^{-1})	88
$(B-R)^a$	-0.18 ± 0.08
u^c (mag)	16.00 ± 0.05
g^c (mag)	15.83 ± 0.05
r^c (mag)	15.87 ± 0.05
i^c (mag)	16.57 ± 0.05
z^c (mag)	16.59 ± 0.10
$A_V{}^d$ (mag)	0.091

Notes. [a]From Gil de Paz, Madore & Pevunova (2003); [b]distance based on the tip of the Red Giant Branch distance from Aloisi et al. (2007); [c]from Brown et al. (2014); [d]Galactic extinction from Schlegel, Finkbeiner & Davis (1998).

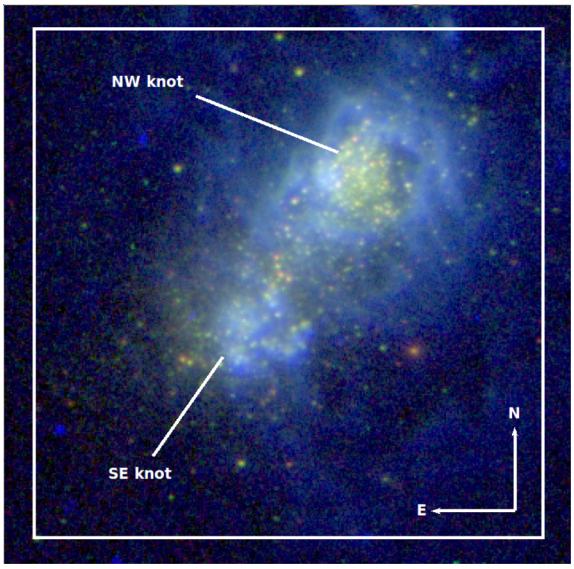

Figure 1. Colour composite *Hubble Space Telescope* image of IZw18 in three bandpasses (blue = WFPC2/F658N, green = WFPC2/F555W, red = WFPC2/F814W, i.e. Hα-V-I). The observed FOV of PMAS (16 × 16 arcsec^2) is represented by the white box. North is up and east is to the left.

The paper is organized as follows. In Section 2, we report observations and data reduction. Flux measurements and emission line intensity maps are presented in Section 3. In Sections 4 and 5, we show the 2D view of the ionization structure and nebular properties, respectively. Section 6 discusses the spatial variation of chemical abundances and physical conditions over our IFU aperture. In Section 7, we present the integrated properties from selected regions of IZw18. Finally, Section 8 summarizes the main conclusions derived from this work.

2 OBSERVATIONS AND DATA REDUCTION

IZw18 was observed in 2012 December, with the IFU Potsdam Multi-Aperture Spectrophotometer (PMAS; Roth et al. 2005, 2010),

attached to the 3.5 m telescope at the Calar Alto Observatory. A grating with 500 grooves per mm was used during the observing night; this provides a spectral range from ∼3640 to 7200 Å with a linear dispersion ∼2 Å pixel^{-1} and an effective spectral resolution of ∼3.6 Å. The observations were performed using the PMAS lens array mode for which the field-of-view (FOV) is formed by 256 fibres. Each fibre has a spatial sampling of 1 × 1 arcsec^2 on the sky resulting in a FOV of 16 × 16 arcsec^2 (∼1.4 kpc × 1.4 kpc at the distance of 18.2 Mpc) (see Fig. 1).

We observed a total of 2.5 h on the galaxy, with the integration time split into six exposures of 1500 s each; sky frames were taken moving the IFU away from the target position in order to provide the sky background emission to be subtracted from the target spectra. All science frames were observed at airmasses ∼1.1 to minimize the effects due to differential atmospheric refraction. Additionally, all necessary calibration frames (exposures of arc lamps and of continuum lamps) were obtained. Observations of the spectrophotometric standard star Feige 34 were obtained throughout the observing night to flux calibrate the data.

The data reduction was performed following the procedure described in Kehrig et al. (2013). We have reduced the IFU data using the P3D (Sandin et al. 2010) and IRAF[2] software. We checked the accuracy of the wavelength calibration by measuring the central wavelength of the [O I] λ5577 Å sky line in all fibres and found a standard deviation of ∼0.30 Å.

3 FLUX MEASUREMENTS AND EMISSION LINE INTENSITY MAPS

In this work, we measure emission line fluxes with the SPLOT routine in IRAF by integrating all the line flux between two points given by the position of a local continuum. The continuum level is estimated by visually placing the graphics cursor at both sides of each line. This process was repeated several times for each emission line by varying the continuum position. We take the mean and the standard deviation of the repeated measurements as the final flux of each line and its associated uncertainty, respectively. The relative errors in the line intensities are typically ∼5 per cent for the bright lines (e.g. Hβ; [O III] λ5007; Hα). Typical uncertainties for the faintest lines ([O III] λ4363; [N II] λ6584; [O I] λ6300) are about ∼15–25 per cent and may reach up to ∼30–40 per cent in some fibres.

Using our own IDL scripts, we combine the line fluxes with the position of the fibres on the sky to create the maps of emission lines presented in this paper. Fig. 2 displays the [O II] λ3727, Hβ, [O III] λ4363, [O III] λ5007, and Hα emission line maps. As a guide to the reader, the spaxel[3] that corresponds to the Hα emission peak is indicated in all maps. The global structure of all the emission line maps is similar, but not all display the same area over the IZw18 FOV. The intensity distribution of Hβ, [O III] λ5007, and Hα is more extended than that of [O II] λ3727 and [O III] λ4363 because those lines are among the brightest optical emission lines in the IZw18 spectra. In the Hα map, we indicated the NW and SE knots, and an arc-like structure (called here 'plume') which has one end rooted in the vicinity of the NW knot. From the maps of Hβ and [O III] λ5007, we can also distinguish these three regions.

The spatial distribution of the emission in [O III] λ4363, Hβ, [O III] λ5007 and Hα is peaked on the NW component while the [O II] λ3727 emission reaches its maximum at the SE component. By inspecting the distribution of the [O III] λ5007 emission line, we can see that its peak intensity in the NW knot is slightly larger than that in the SE knot. In the case of the [O III] λ4363, Hβ and Hα maps, the ratio between the peak intensities from the NW knot and those from the SE knot is ∼1.3–1.5, with the highest ratio found for the [O III] λ4363 map.

The reddening coefficient corresponding to each spaxel, c(Hβ), was computed from the ratio of the measured-to-theoretical Hα/Hβ assuming the reddening law of Cardelli, Clayton & Mathis (1989), and case B recombination with electron temperature T_e = 2×10^4 K and electron density n_e = 100 cm^{-3} which give an intrinsic value of Hα/Hβ = 2.75 (Osterbrock & Ferland 2006).

Typical values of the absorption Hβ equivalent width, EW(Hβ)$_{abs}$, found for line-emitting SF galaxies are in the range ∼0–2 Å (e.g. McCall, Rybski & Shields 1985; Cairós et al. 2009b; Pérez-Montero et al. 2009). Considering the high values for EWs of Balmer emission lines measured from our data [e.g. EW(Hβ) ∼ 40–500 Å], the effect of the underlying stellar population in these lines appears not to be important. If we adopted an EW(Hβ)$_{abs}$ ∼2 Å, the underlying absorption correction would be typically small, less than 5 per cent in Hβ.

4 SPATIALLY RESOLVED IONIZATION STRUCTURE

Maps of some of the relevant line ratios which are indicators of the ionization structure for ionized gaseous nebulae are displayed in Fig. 3. These line ratios are corrected for reddening using the corresponding c(Hβ) for each spaxel.

The spatial distribution of the abundance indicator R_{23} = ([O II] λ3727+[O III] λλ4959,5007)/Hβ, first introduced by Pagel et al. (1979) and afterwards calibrated by several authors (e.g. McCall et al. 1985; McGaugh 1991), is found to be relatively flat without any significant peak (see the map of R_{23} in Fig. 3). However, the commonly used ionization parameter diagnostic [O III]/[O II][4] does not show a homogeneous spatial distribution with the highest values of [O III]/[O II] found within the NW knot (see the corresponding map in Fig. 3). Fig. 4 shows the relation between the measured values of R_{23} and [O III]/[O II] from which it is clear that there is no dependence between R_{23} and the ionization parameter (as traced by [O III]/[O II]) across IZw18 (see also Vílchez & Iglesias-Páramo 1998). While R_{23} remains practically constant (0.40 ≤ log R_{23} ≤ 0.55), [O III]/[O II] presents changes larger than a factor of 8 across the FOV. The observations of the giant H II region NGC 604 by Diaz et al. (1987) give another example where a large range of excitation is seen whereas the metallicity indicator R_{23} remains substantially constant (see also Pérez-Montero et al. 2011). In Section 6 we will discuss the observed variations of R_{23} and [O III]/[O II] from a statistical point of view.

In the maps shown in Fig. 3, high values of [O III]/[O II] and [O III] λ5007/Hβ, and low values of [S II] λλ6717,6731/Hα and [N II] λ6584/Hα correspond to the areas of ionized gas with relatively high excitation. By inspecting these maps, there is a clear

[2] IRAF is distributed by the National Optical Astronomical Observatories, which are operated by the Association of Universities for Research in Astronomy, Inc., under cooperative agreement with the National Science Foundation.

[3] Individual elements of IFUs are often called 'spatial pixels' (commonly shortened to 'spaxel'); the term is used to differentiate between a spatial element on the IFU and a pixel on the detector.

[4] [O III]/[O II] = (4959+5007)/3727.

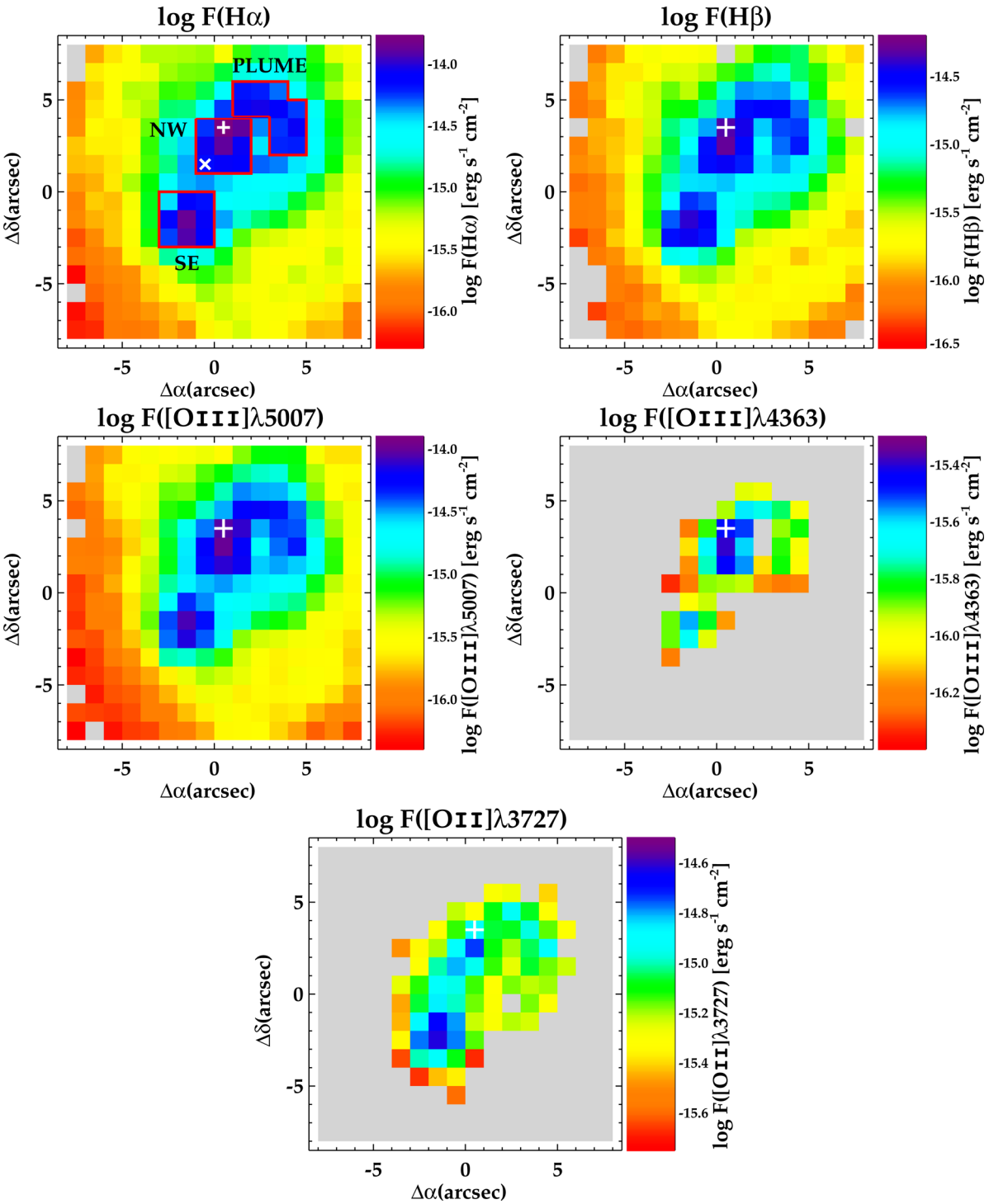

Figure 2. Emission line flux maps of IZw18: [O II] λ3727, Hβ, [O III] λ4363, [O III] λ5007, Hα. The spaxels with no measurements available are left grey. All maps are presented in logarithmic scale. As a guide to the reader, the peak of Hα emission is marked with a plus (+) sign on all maps. The cross on the Hα map marks the spaxel where we detect the WR feature (see Section 4). The Hα map also shows the boundaries of the areas that we use to create the integrated spectra of the NW and SE knots, and of the 'plume' region (see text for details). North is up and east to the left.

tendency for the gas excitation to be higher at the location of the NW knot and thereabouts, in comparison to the SE component. Here we should also note that Kehrig et al. (2015) found the NW component to be very close to the nebular He IIλ4686-emitting region (see fig. 2 from Kehrig et al. 2015). All this indicates the presence of a harder ionizing field in the NW knot of IZw18. We will discuss more about it in Section 5. Another feature of the ionization structure in IZw18 is the existence of a relatively high-excitation diffuse gas outside of the main SF knots indicated by an extended low surface brightness emission in the maps of [O III] λ5007/Hβ.

The standard diagnostic diagrams (Baldwin, Phillips & Terlevich 1981, hereafter BPT) are a powerful tool, widely used to identify the dominant mechanism of gas excitation, i.e. either

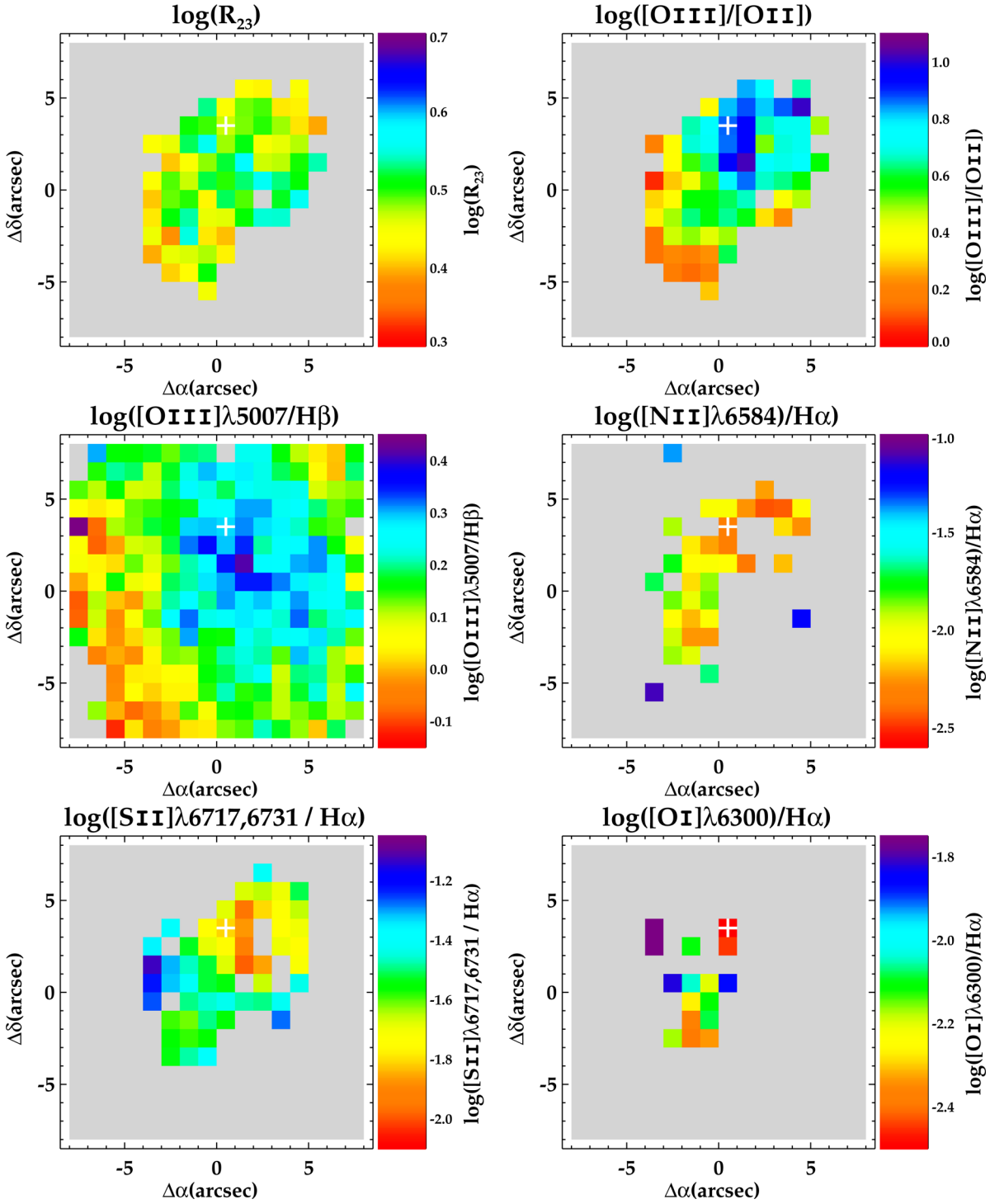

Figure 3. Line ratio maps of IZw18: R_{23}, [O III]/[O II], [O III] λ5007/Hβ, [N II] λ6584/Hα, [S II] λ6717,6731/Hα, [O I] λ6300/Hα. The spaxels with no measurements available are left grey. All maps are presented in logarithmic scale. As a guide to the reader, the peak of Hα emission is marked with a plus (+) sign on all maps. North is up and east to the left.

photoionization by massive stars within H II regions or other ionizing sources, including photoionization by AGNs, post-AGB stars and shocks (e.g. Kehrig et al. 2012; Gomes et al. 2016; Sánchez et al. 2015). The BPT diagrams, on a spaxel-by-spaxel basis, for IZw18 are shown in Fig. 5: [O III] λ5007/Hβ versus [N II] λ6584/Hα, [S II] λλ6717,6731/Hα, and [O I] λ6300/Hα. The line ratios obtained from the one-dimensional (1D) spectra of selected regions across our FOV (see Section 7 and Table 3) are overplotted on the BPT diagrams. For all positions in IZw18 our emission line ratios fall in the general locus of SF objects according to the spectral classification scheme proposed by Kewley et al. (2001) and Kauffmann et al. (2003), as indicated in Fig. 5. This suggests that photoionization from hot massive stars is the dominant excitation mechanism within IZw18.

Regarding the massive stellar content of IZw18, previous optical long-slit spectroscopy detected Wolf–Rayet (WR) features (most

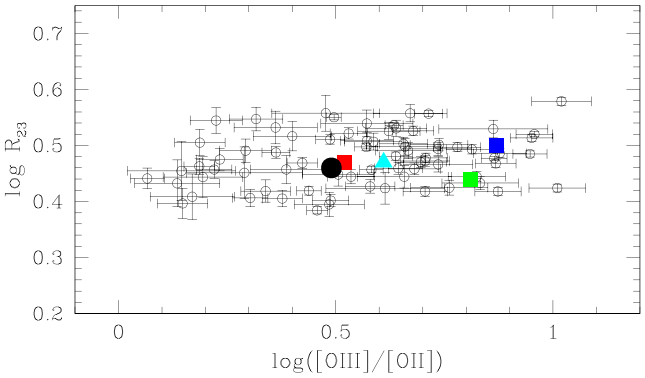

Figure 4. The relation between log R_{23} and log([O III]/[O II]). Open circles correspond to individual spaxels from the data cube. Overplotted as blue, red, and green squares are the line ratios measured from the 1D spectra of the NW knot, SE knot and 'plume', respectively; the cyan triangle shows the line ratio values from the total integrated spectrum of IZw18; the black circle corresponds to the line ratios from the spectrum of the 'halo' of IZw18 (see Section 7 and Table 3 for details on the 1D spectra extracted for selected galaxy regions).

commonly a broad feature centred at ∼4680 Å or 'blue bump') in the NW region (e.g. Izotov et al. 1997; Legrand et al. 1997). However, the uncertainty on the exact location of the slits has prevented these works to give the WR star's position more precisely. Our data set shows indications of a weak WR blue bump around ∼4650–4730 Å in one spaxel (see Fig. 6), which lies in the NW knot; more specifically it is found to be ∼1.5 arcsec (∼130 pc at the distance of IZw18) SE of the Hα peak (see the Hα flux map in Fig. 2). We cannot discard the presence of even fainter WR features at other locations across our FOV which might not be detected due to the signal-to-noise ratio of our spectra. The observation of WRs in very metal-deficient objects, like IZw18, keeps challenging current stellar evolutionary models for single massive stars, which do not predict any WRs in metal-poor environments (e.g. Leitherer et al. 2014). Further investigation on formation channels for such metal-poor WRs is needed but is beyond the scope of this work (see e.g. Crowther 2007, and references therein).

5 A 2D VIEW OF THE PHYSICAL–CHEMICAL PROPERTIES FOR THE IONIZED GAS

In order to derive the physical properties and ionic abundances of the ionized gas for IZw18, we have used the expressions given by Pérez-Montero (2014) which are obtained from the code PYNEB (Luridiana, Morisset & Shaw 2014). We have calculated the final errors in the derived quantities by error propagation and taking into account errors in flux measurements.

For more than 80 per cent of the spectra where we measure the [S II] λ6717/λ6731 line ratio, the derived n_e values are $\lesssim$300 cm^{-3}, which place most of spaxel spectra in the low-density regime.

For the [O III] λ4363-emitting spaxels, we have derived the T_e values of [O III] using the [O III] λ4363/[O III] λ4959,5007 line ratio, corrected for extinction. We were able to measure the faint auroral line [O III] λ4363 above the 3σ detection limit for 44 spaxels. These spaxels cover a projected area of nearly 42 arcsec^2 equivalent to 0.32 kpc^2, including the NW knot and a portion of the SE component (see the map of [O III] λ4363 in Fig. 2). The left panel of Fig. 7 displays the distribution of the [O III] electron temperature which shows values going from near 15 000 K to $\gtrsim$22 000 K; here it is the first time that T_e[O III] values $\gtrsim$22 000 K are derived for

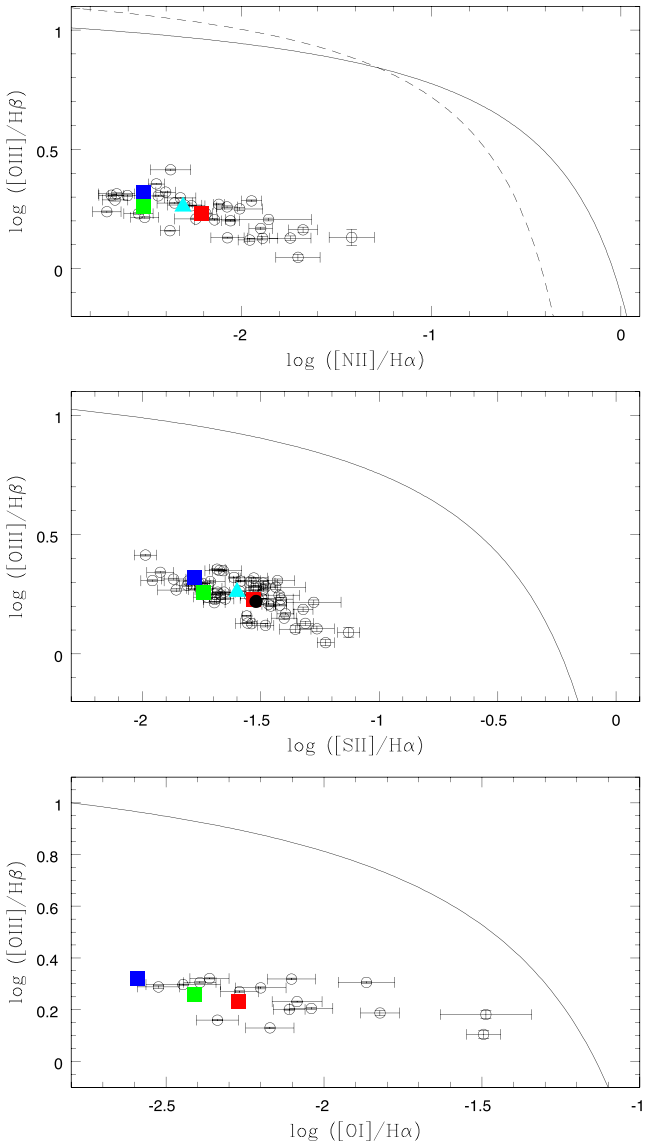

Figure 5. BPT diagnostic diagrams for IZw18. From top to bottom: log ([O III] λ5007/Hβ) versus log ([N II] λ6584/Hα), log ([O III] λ5007/Hβ) versus log ([S II] λ6731,6717/Hα) and log ([O III] λ5007/Hβ) versus log ([O I] λ6300/Hα). The symbols are as described in Fig. 4. Overplotted as a black solid curve (in all three panels) is the theoretical maximum starburst model from Kewley et al. (2001), devised to isolate objects whose emission line ratios can be accounted for by the photoionization by massive stars (below and to the left of the curve) from those where some other source of ionization is required. The black-dashed curve in the [N II] λ6584/Hα diagram represents the demarcation between SF galaxies (below and to the left of the curve) and AGNs defined by Kauffmann et al. (2003).

IZw18. Such high values of T_e[O III] are rarely found in nearby H II galaxies/H II regions (e.g. Pérez-Montero & Contini 2009).

In active SF regions, stellar winds from massive stars and/or supernovae remnants will likely produce shock-waves. As for IZw18, the complex geometry of its ionized gas argue in favour of a contribution due to shocks (e.g. Hunter & Thronson 1995; Cannon et al. 2002). Thus a shock-contamination on emission lines cannot be ruled out. One of the effects of shock-waves is to increase the [O III] λ4363/[O III] λ5007 ratio, and therefore the T_e[O III] (e.g. Peimbert, Sarmiento & Fierro 1991). As T_e[O III] $\gtrsim$ 20 000 K is more typical of shock-heated nebulae than of SF regions (e.g. Blair, Kirshner

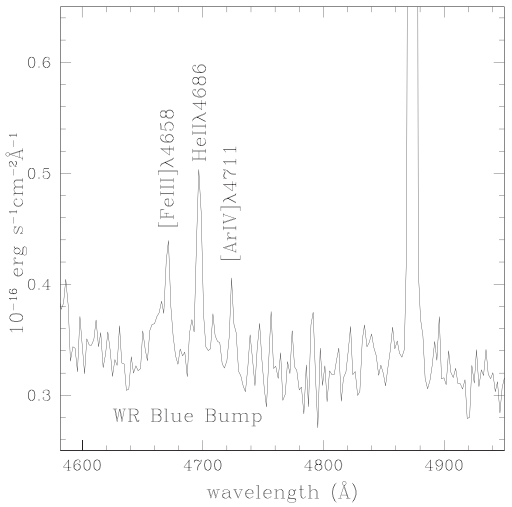

Figure 6. Spectrum showing signs of a faint, broad underlying emission feature around ∼4650–4730 Å, i.e. the WR blue bump. The location of the WR feature within our FOV is indicated in the Hα map from Fig. 2. The narrow [Fe III] λ4658, He IIλ4686, and [Ar IV] λ4711 emission lines are marked.

& Chevalier 1981; Kehrig et al. 2011), initially one could guess that our highest values of T_e[O III] are, in part, the result of shock excitation. However, observational arguments reason against a significant shock component to our data. We find no evidence for [S II]/Hα and/or [O I]/Hα enhancement (a usual sign of shock excitation; e.g. Skillman 1985; Dopita & Sutherland 1996) associated with the higher-T_e[O III] spaxels (see Figs 3 and 7); actually, most of the [O I] emission is concentrated on the SE knot where we found relatively lower values of T_e[O III] (see Fig. 7). Besides, the BPT diagrams in Fig. 5 indicate that shocks do not play an important role in the gas excitation (see Section 4). So the enhanced [O III] temperatures derived are expected to be associated primarily with photoionization from hot massive stars, and any possible contribution to the T_e[O III] errors due to shocks should be negligible.

It is well known that in the process of flux measurement of very faint emission lines, like [O III] λ4363, a bias (e.g. continuum fitting) is expected to overestimate line intensities (e.g. Rola & Pelat 1994; Kehrig et al. 2004). To check if such a bias is affecting our [O III] λ4363 flux, we plot the relation between T_e[O III] and the relative error measured for the [O III] λ4363 line in the right panel of Fig. 7, which shows no systematic effect. This indicates that the highest values of T_e[O III] that we compute are real and not an effect of an overestimation during the measurement of the [O III] λ4363 flux. Note that we also derive lower values of T_e[O III] ∼16 000–18 000 K outside the two central knots, consistent with results reported in previous work (e.g. Vílchez & Iglesias-Páramo 1998). All this supports the robustness of our measurements of the [O III] λ4363 line used to derive T_e[O III].

For the low-excitation zone, no auroral line (e.g. [O II] λ7320,7330; [N II] λ5755) could be measured in any spaxel. In our case, the values of T_e[O II] were calculated from the empirical relation between [O II] and [O III] electron temperatures given by Pilyugin, Vílchez & Thuan (2006). This relation has been successfully used to calculate T_e[O II] in other H II galaxies (e.g. Kehrig et al. 2008; Cairós et al. 2009a, 2010).

The oxygen ionic abundance ratios, O^+/H^+ and O^{2+}/H^+, were derived from the [O II] λ3727 and [O III] $\lambda\lambda$ 4959,5007 lines, respectively, using the corresponding electron temperatures. A small fraction of the unseen O^{3+} ion is expected to be present in H II regions that show high-ionization emission lines like He IIλ4686 in their spectra. According to the photoionization models from Izotov et al. (2006), the O^{3+}/O ratio is $>$ 1 per cent only in the highest-excitation H II regions for which $O^+/(O^+ + O^{2+}) < 10$ per cent. We have checked that for all He IIλ4686-emitting spaxels,[5] $O^+/(O^+ + O^{2+})$ is higher than 10 per cent, so the total oxygen abundance is assumed to be: $O/H = O^+/H^+ + O^{2+}/H^+$. The map and histogram of the derived oxygen abundance are displayed in Fig. 8. The calculated values of 12+log(O/H) vary approximately between 6.90 and 7.35, with more than 60 per cent of the spaxels showing oxygen abundances in the range of ∼7.0–7.2.

As mentioned above, we see differences of up to ∼10 000 K among our T_e[O III] measurements (see Fig. 7). At first, one can think that such change in T_e[O III] might be mainly the result of differences in the metallicity across IZw18. However, although some degree of O/H variations are observed when considering individual spaxels (see Fig. 8), we find that such variations are not statistically significant, and that the ionized gas of IZw18 is chemically homogeneous over spatial scales of hundreds of parsecs (see Section 6 for details). This points out that the observed difference in T_e[O III] should be mostly due to changes in the ionizing radiation field. Actually, close inspection of Fig. 7 indicates that most of the largest values of T_e[O III] are located in the northwestern region of IZw18, where we find the gas excitation and the ionization parameter (as traced by [O III]/[O II]) to be higher too (see Section 4). It is worth mentioning that the [O III]/[O II] ratio also depends on the effective temperature of the ionizing source(s) so that [O III]/[O II] is larger for higher effective temperatures (e.g. Vilchez & Pagel 1988; Pérez-Montero & Díaz 2005). Also, Fig. 9 shows that there is a general trend for the line ratio indicator of the T_e[O III] to go up when the [O III]/[O II] ratio increases. The fact that the youngest ionizing stars of IZw18 are mostly concentrated in the NW portion (e.g. Contreras Ramos et al. 2011) supports these results. Additionally, Kehrig et al. (2015) report the presence of an extended emission in the high-excitation He IIλ4686 line which is spatially associated with the NW cluster. These authors claim that peculiar very hot, (nearly) metal-free ionizing stars are needed to account for the total He II-ionization budget in IZw18. Moreover, we note here that more than 70 per cent of the spaxels with T_e[O III] $\gtrsim$ 22 000 K are He II-emitting spaxels too. These facts reinforce the existence of a harder ionizing radiation field at the location of the NW SF knot and thereabouts.

6 ANALYSIS OF THE SPATIAL VARIATION OF PHYSICAL CONDITIONS AND CHEMICAL ABUNDANCES

Here, we make use of a statistical analysis to study the spatial variation of properties of the ionized gas across our FOV. We assume that a certain physical–chemical property is homogeneous over IZw18 if two conditions are satisfied: for the corresponding data set (i) the null hypothesis (i.e. the data come from a normally distributed population) of the Lilliefors test (Lilliefors 1967) cannot be rejected at the 10 per cent significance level, and (ii) the observed variations of the data distribution around the single mean value can be explained by random errors, i.e. the corresponding Gaussian sigma ($\sigma_{\rm Gaussian}$) should be lower or of the order of the typical uncertainty of the property considered; we take as typical uncertainty the square

[5] The map of He IIλ4686 is shown in fig. 2 from Kehrig et al. (2015).

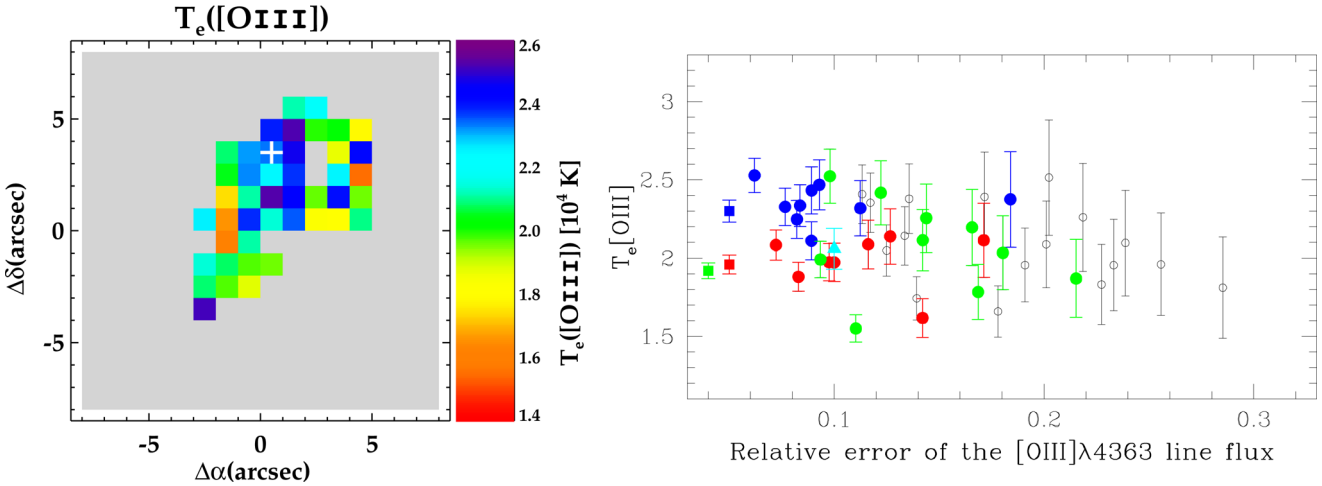

Figure 7. Left panel: map of T_e[O III] derived directly from the measurement of the [O III] λ4363 line flux. The spaxels with no measurements available are left grey. The peak of Hα emission is marked with a plus (+) sign for orientation. North is up and east to the left. Right panel: T_e[O III] derived directly from the measurement of the [O III] λ4363 line flux versus the relative error of the measurement. Open circles represent individual spaxels; blue, red and green circles indicate the individual spaxels used to create the 1D spectra of the NW knot, SE knot, and plume, respectively. Squares indicate the values measured from the 1D integrated spectra with the same colour-code as used for the individual spaxels. The cyan triangle shows the value measured from the IZw18 integrated spectrum (see Section 7 and Table 3 for details on the 1D spectra extracted for selected galaxy regions).

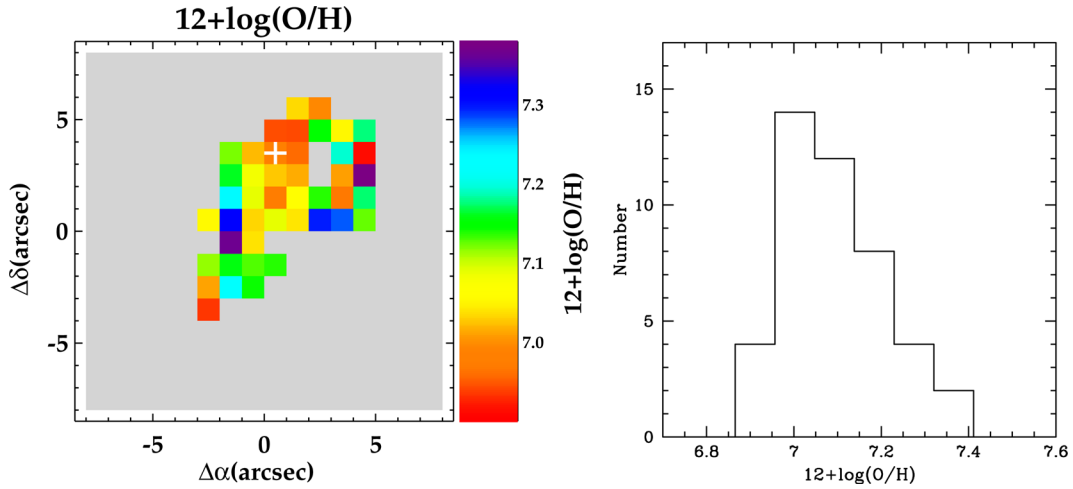

Figure 8. Left panel: map of oxygen abundance (12+log O/H) derived from T_e[O III]. The corresponding histogram is in the right panel.

root of the weighted sample variance ($\sigma_{\rm weighted}$). Previous work has successfully applied this method to the analysis of abundances and physical conditions in H II galaxies (see Pérez-Montero et al. 2011; Kehrig et al. 2013; Pérez-Montero et al. 2013). Table 2 displays the results from our statistical analysis for several relevant ISM properties.

From Table 2, we can see that the distribution of the measured values for T_e[O III], O/H, [O III]/[O II] and R_{23}, from individual spaxels, can be represented by a Gaussian fit in agreement with the Lilliefors test (i.e. the corresponding significance levels for such distributions are $>$ 10 per cent). Despite that, in the case of the T_e[O III] and of the [O III]/[O II] ratio, we find that $\sigma_{\rm Gaussian} > \sigma_{\rm weighted}$. This points out that the T_e[O III] and [O III]/[O II] values are not homogeneously distributed across IZw18, and that, at first order, random variables alone could not explain the distribution observed of these two ISM properties. This result gives support to the existence of an electron temperature gradient in IZw18 as suggested by Izotov & Thuan (1999) from their long-slit spectroscopic analysis of the NW and SE components (see also Vílchez & Iglesias-Páramo 1998).

Regarding the O/H spatial distribution, the two conditions for a given property to be considered homogeneous, as mentioned above, are accomplished: the derived values of O/H are fitted by a normal distribution according to the Lilliefors test, and the corresponding $\sigma_{\rm Gaussian}$ is of the order of $\sigma_{\rm weighted}$. Our results, therefore, show that the ionized gas-phase O/H remains mostly uniform over spatial scales of hundreds of parsecs. This confirms that there is no significant abundance gradient nor measurable discontinuity in IZw18, as it has been suggested in previous work (Vílchez & Iglesias-Páramo 1998; Legrand et al. 2000). Here, we assume that the representative metallicity of IZw18 is 12+log(O/H) = 7.11 ± 0.01 (∼1/40 of the solar metallicity) which represents the derived error-weighted mean value of O/H and its corresponding statistical error from all the individual spaxel O/H abundances obtained using the direct method with electron temperature measurement (for this O/H distribution, the square root of the weighted sample variance associated is 0.12 dex; see Table 2). The observed absence of significant metallicity difference among the areas near the two main SF knots and the gas located farther out impose strong constrains for the mechanisms that

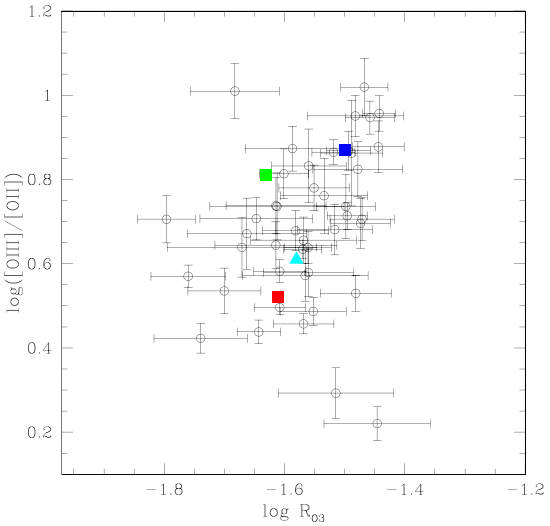

Figure 9. Log ([O III]]/[O II]) versus log R_{O3} [= log ([O III] λ4363/[O III] λ4959,5007)], i.e. the relation between the line ratio indicators of the ionization parameter and electron temperature. The symbols are as described in Fig. 4.

Table 2. Results from the statistical analysis for the distribution of the physical–chemical conditions in the ISM across the PMAS FOV of IZw18.

	Statistical properties				
	$\mu_{\rm weighted}{}^a$	$\sigma_{\rm weighted}{}^b$	$\mu_{\rm Gaussian}{}^c$	$\sigma_{\rm Gaussian}{}^d$	Sign.(per cent)^e
$T_{\rm e}$([O III]) (K)	21 300	2400	22 400	4180	36
12+log(O/H)	7.11	0.12	7.06	0.14	34
log([O III]/[O II])	0.55	0.24	0.60	0.33	25
log(R_{23})	0.47	0.05	0.47	0.06	50

Notes. (a) Error-weighted mean; (b) square root of the weighted sample variance associated with the corresponding weighted mean; (c) mean of the Gaussian distribution; (d) standard deviation of the Gaussian distribution; (e) significance level of the null hypothesis in the Lilliefors test (see the text for details).

triggered star formation and also for the chemical evolution history of IZw18. The H II regions in IZw18 should have evolved along a similar enrichment scenario over the whole scale of the galaxy in order to produce the observed chemically homogeneous ISM (e.g. Kunth, Matteucci & Marconi 1995; Roy & Kunth 1995; Vílchez & Iglesias-Páramo 1998).

Following the same statistical analysis, the behaviour of the R_{23} distribution is observed to be similar to that of the oxygen abundance, i.e. the R_{23} parameter seems to be very uniform across IZw18, thus being insensitive to possible effects from changes in the hardness of the ionizing radiation and the ionization parameter (as traced by [O III]/[O II]). This result indicates that R_{23} can be considered as a good metallicity indicator in metal-poor SF galaxies (see e.g. Pagel et al. 1979; Vilchez 1995; Pilyugin 2000; James et al. 2016). Indeed, the constant metallicity derived over the entire scale of IZw18, despite the non-homogeneous distribution in the degree of ionization observed, clearly shows its independence from the ionization parameter (see also Section 4).

7 PROPERTIES OF SELECTED REGIONS OF IZW18 FROM INTEGRATED SPECTRA

We also take advantage of our IFU data to simulate the 1D spectra of selected galaxy regions. The representative spectra of the NW and SE knots, and of the 'plume' region, were constructed by adding the flux in the spaxels within each of the corresponding areas whose boundaries are displayed on the Hα map in Fig. 2. For both the NW and SE knots, the area of their aperture extraction is of 3 × 3 arcsec^2; the 'plume' integrated region corresponds to an area of ∼12 arcsec^2. In addition, we have created a 1D spectrum representative of the gaseous ionized 'halo' of IZw18. To do so we have integrated the flux in all the spaxels for which the Hα flux measurements present a relative error $\gtrsim$20 per cent; thus exclusively the emission of the fainter ionized gas ('halo') has been integrated in the halo spectrum. We also obtained, for the first time, the IZw18 integrated spectrum by summing the emission from each spaxel within an area of ∼168 arcsec^2 (∼1.3 kpc^2 at the distance of 18.2 Mpc), enclosing basically all the nebular emission across our FOV. Considering IZw18 as an excellent local analogue of primeval systems, the analysis of its integrated properties may be important for the study of intermediate-/high-redshift SF galaxies for which only their integrated characteristics are known due to their distance (e.g. Kewley et al. 2013; Nakajima et al. 2013).

Fig. 10 presents the 1D spectra for the aforementioned regions of IZw18. The emission line fluxes and c(Hβ) corresponding to each summed spectra were measured following the same procedure as in Section 3. For the integrated spectra, we derived the physical conditions and oxygen abundances as described in Section 5 for individual spaxels. The nitrogen ionic abundance ratio, N^+/H^+, was calculated from the PYNEB-based expression given by Pérez-Montero (2014), using the [N II] λ6584 emission line and assuming $T_{\rm e}$[N II] ∼$T_{\rm e}$[O II]; the N/O abundance ratio was computed under the assumption that N/O = N^+/O^+, based on the similarity of the ionization potentials of the ions involved. Reddening-corrected line intensities, normalized to Hβ, along with the physical–chemical properties derived from the integrated spectra are shown in Table 3.

The measurements of the integrated line ratios [O III] λ5007/Hβ, [N II] λ6584/Hα, [S II] λ6717,6731/Hα and [O I] λ6300/Hα place all the selected regions on the SF zone of the BPT diagrams (see Fig. 5). The comparison among the values for the integrated [O III]/[O II] ratios shows that the NW knot and 'plume' spectra present [O III]/[O II] higher than the ratios derived for the other regions (see Table 3). This result is consistent with the presence of a harder ionizing radiation field near the northwestern area of IZw18, as discussed in Section 5.

The $T_{\rm e}$[O III] and O/H derived for the NW and SE components are consistent, within the errors, with those obtained by Izotov & Thuan (1999) through long-slit spectroscopy along the NW–SE knots. In comparison with the values of 12 + log(O/H) from Skillman & Kennicutt (1993) and Vílchez & Iglesias-Páramo (1998), our oxygen abundances ([O III] electron temperatures) are somewhat lower (higher) than theirs. The discrepancy between our values and those previously obtained based on long-slit spectroscopy may be due to their spectra covering partially different regions due to slit position and orientation. Table 4 summarizes, for both the NW and SE knots, the $T_{\rm e}$[O III] and O/H measurements derived here and those formerly reported in the references mentioned above.

By comparing the different electron temperature values from Table 3, we find that the NW knot shows a relatively higher temperature, in agreement with the observed spatial distribution of $T_{\rm e}$[O III] (see Section 5). Regarding the oxygen abundances, the SE knot, 'plume' and IZw18 integrated spectra give equivalent values considering the corresponding error bars; the NW knot presents a barely lower O/H. Remarkably, however, we note that 12+log(O/H) derived from all selected region spectra agree with each other within ∼0.10 dex which is of the order of $\sigma_{\rm weighted}$ (see Tables 2 and 3).

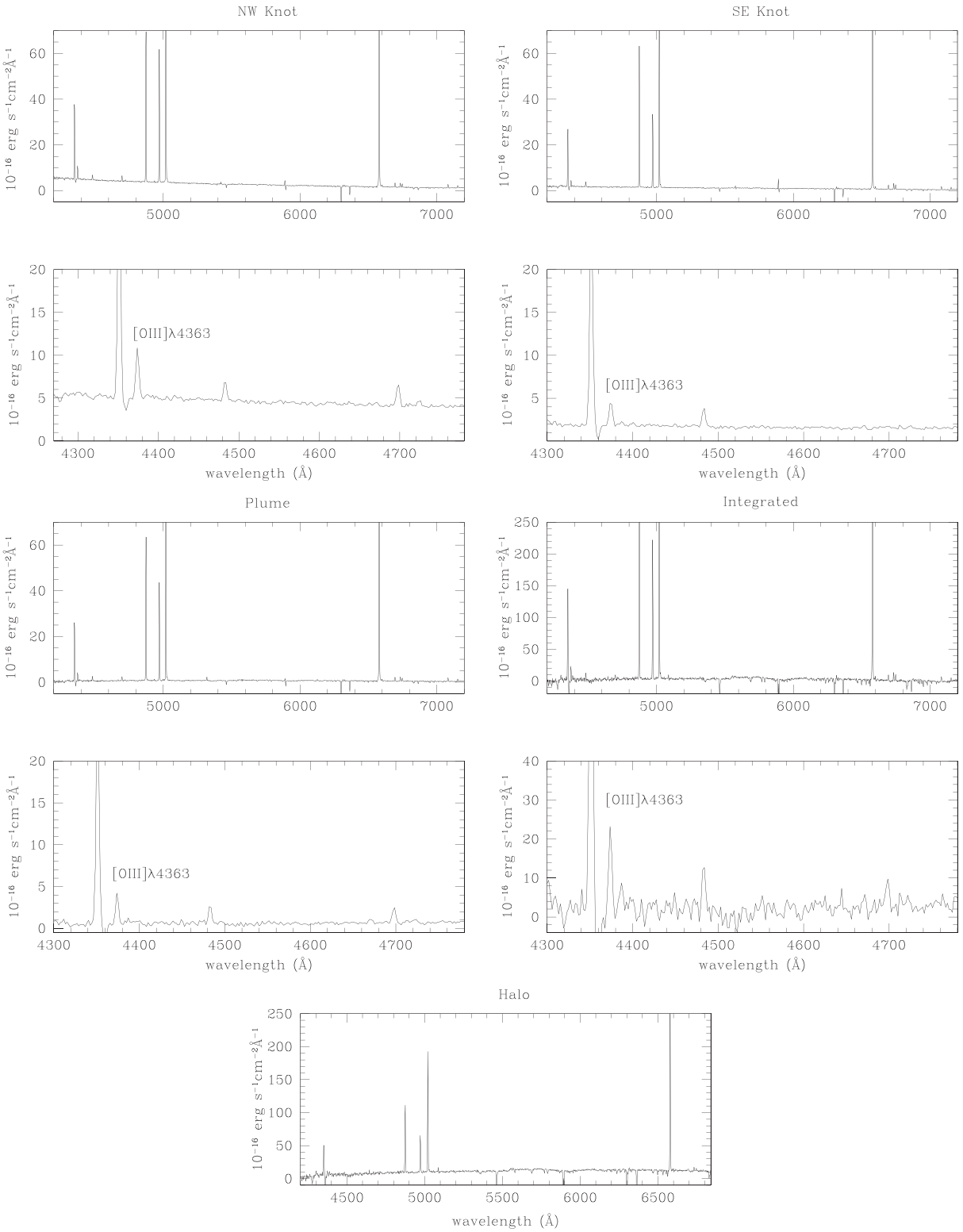

Figure 10. Flux-calibrated 1D spectra of the selected regions of IZw18 (see the text for details). A zoom of the wavelength range ∼4300–4700 Å showing the temperature sensitive emission line [O III] λ4363 for the NW knot, SE knot, 'plume' region and IZw18 integrated is also displayed. The spectra are in units of 10^{-16} erg s^{-1} cm^{-2} Å^{-1}.

This means that the integrated-spectrum metallicity [12+log (O/H) $= 7.10 \pm 0.03$] is consistent with the O/H from the other selected regions (which cover smaller areas) and with the representative metallicity of IZw18 based on spaxel-by-spaxel measurements as defined previously in Section 6. Thus, our IFS study shows that O/H of IZw18 does not depend on the aperture size used and that the IZw18 integrated spectrum can reliably represent the metallicity of its ionized ISM.

With respect to the nitrogen abundance, we find that all the selected regions of IZw18 present similar N/O ratios within the

Table 3. De-reddened emission line fluxes relative to 1000·I(Hβ) and physical properties from different selected regions.

Wavelength (Å)	NW knot	SE knot	'Plume'	'Halo'	Integrated
3727 [O II]	374 ± 16	678 ± 21	372 ± 25	714 ± 40	581 ± 50
3868 [Ne III]	179 ± 6	145 ± 5	128 ± 8	–	101 ± 17
4340 Hγ	526 ± 8	488 ±4	467 ± 4	476 ± 18	490 ± 7
4363 [O III]	87 ± 4	55 ± 3	56 ± 2	–	63 ± 6
4471 He I	34 ± 1	38 ± 2	36 ± 3	–	38 ± 4
4686 He II	40 ± 3	–	34 ± 3	–	23 ± 4
4714 [Ar IV]	9 ± 2	–	–	–	–
4861 Hβ	1000 ± 1	1000 ± 4	1000 ± 6	1000 ± 15	1000 ± 7
4959 [O III]	741 ± 13	605 ± 6	629 ± 7	555 ± 10	625 ± 8
5007 [O III]	2093 ± 10	1697 ± 19	1787 ± 16	1650 ± 29	1800± 21
6300 [O I]	7 ± 1	15 ± 1	11 ± 2	–	–
6312 [S III]	6 ± 1	6 ± 1	7 ± 1	–	–
6563 Hα	2750 ± 7	2750 ± 14	2750 ± 17	2576 ± 37	2750 ± 20
6584 [N II]	8.39 ± 0.60	17 ± 1	8.30 ± 0.40	–	13 ± 2
6678 He I	27 ± 1	30 ± 2	28 ± 2	–	29 ± 2
6717 [S II]	26 ± 1	46 ± 2	29 ± 2	52 ± 4	41 ± 2
6731 [S II]	20 ± 1	34 ± 2	20 ± 2	27 ± 4	28 ± 3
7065 He I	24 ± 1	25 ± 1	25 ± 1	–	27 ± 2
7135 [Ar III]	17 ± 1	16 ± 1	16 ± 2	–	16 ± 3
c(Hβ)	0.13	0.13	0.09	0.00	0.04
−EW(Hβ) (Å)	76	150	320	23	350
F(Hβ) (erg s^{-1} cm^{-2})	3.95×10^{-14}	3.23×10^{-14}	3.16×10^{-14}	4.50×10^{-14}	1.59×10^{-13}
F(Hα) (erg s^{-1} cm^{-2})	1.09×10^{-13}	8.87×10^{-14}	8.70×10^{-14}	1.16×10^{-13}	4.36×10^{-13}
log (R_{23})	0.50	0.47	0.44	0.46	0.47
log ([O III]/[O II])	0.87	0.52	0.81	0.49	0.61
log ([O I]6300/Hα)	−2.59	−2.27	−2.41	–	–
log ([N II]6584/Hα)	−2.52	−2.21	−2.52	–	−2.31
log ([S II]6717+6731/Hα)	−1.78	−1.53	−1.74	−1.52	−1.60
log ([O III]5007/Hβ)	0.32	0.23	0.26	0.22	0.26
n_e([S II])(cm^{-3})	110	<100	<100	<100	<100
T_e([O III]) (K)	23000 ± 700	19600 ± 600	19200 ± 500	–	20600 ± 1300
T_e([O II])^a (K)	19200 ± 500	16700 ± 500	16400 ± 400	–	17400 ± 900
12+log(O^{++}/H^+)	6.96 ± 0.02	7.01 ± 0.02	7.05 ± 0.02	–	6.99 ± 0.04
12+log(O^+/H^+)	6.17 ± 0.03	6.59 ± 0.03	6.35 ± 0.04	–	6.47 ± 0.06
12+log(O/H)$_{T_e}$^{b}	7.03 ± 0.02	7.15 ± 0.02	7.13 ± 0.02	–	7.10 ± 0.03
12+log(N^+/H^+)	4.65 ± 0.03	5.06 ± 0.03	4.76 ± 0.03	–	4.92 ± 0.06
log(N/O)$_{T_e}$^{c}	−1.52 ± 0.05	−1.53 ± 0.04	−1.58 ± 0.04	–	−1.55 ± 0.09

Notes. $^a T_e([O\,II]) = 0.72 \times T_e([O\,III]) + 0.26$ (Pilyugin et al. 2006).
^{b}O/H = ($O^+/H^+ + O^{2+}/H^+$).
^{c}N/O = N^+/O^+.

Table 4. Summary of [O III] electron temperatures and oxygen abundances for the NW and SE components.

Property	NW knot	SE knot	Reference*
T_e([O III]) (K)	19600 ± 900	17200 ± 1200	1
	20300 ± 700	17700 ± 600	2
	21500 ± 1400	19500 ± 800	3
	23000 ± 700	19600 ± 600	4
12+log(O/H)$_{T_e}$	7.17 ± 0.04	7.26 ± 0.05	1
	7.16 ± 0.05	7.32 ± 0.08	2
	7.07 ± 0.05	7.17 ± 0.06	3
	7.03 ± 0.02	7.15 ± 0.02	4

*References: (1) Skillman & Kennicutt (1993); (2) Vílchez & Iglesias-Páramo (1998); (3) Izotov & Thuan (1999); (4) This work.

uncertainties (see Table 3). The N/O values computed here match the characteristic N/O [-log(N/O) ∼1.5–1.6] observed for low-metallicity systems which form the well-known N/O plateau (e.g. Izotov & Thuan 1999; Mollá et al. 2006; Pérez-Montero et al. 2011). Additionally, we checked that the N/O ratios for the NW and SE knots agree with those reported in previous studies (e.g. Skillman & Kennicutt 1993; Vílchez & Iglesias-Páramo 1998; Izotov & Thuan 1999).

8 SUMMARY AND CONCLUSIONS

We have analysed PMAS-IFU integral field spectroscopy of IZw18, an extremely low metallicity galaxy, which is our best local laboratory for probing the conditions dominating in distant metal-poor starbursts. These data map the entire spatial extent of the IZw18 main body plus an important region of the extended ionized gas, providing us with a new 2D view of the ionized ISM in IZw18. Maps for the spatial distribution of relevant emission lines and of physical–chemical properties for the ionized gas have been created and analysed. We believe that our observations provide a useful test-bench for realistic photoionization models at the lowest metallicity regime.

Our spaxel-by-spaxel analysis indicates that despite the observed large range of values (∼0.0 to 0.9 dex) for the log [O III]/[O II] ratio (widely used as an ionization parameter indicator), the metallicity

index R_{23} remains substantially uniform; no dependence between R_{23} and the ionization parameter is seen in IZw18. The BPT diagrams, [N II] λ6584/Hα, [S II] λ6717,6731/Hα, and [O I] λ6300/Hα, for the spatially resolved emission lines, indicate that photoionization by massive stars is the dominant excitation source for the gas within our FOV. We have detected a very faint blue bump of WR stars towards the NW knot. Regions with higher excitation and harder ionizing radiation are preferentially located towards the NW zone of IZw18 where we find the largest values of T_e[O III] too. Also, the NW component is spatially related to an extended He IIλ4686-emitting region that has been proposed to indicate the presence of peculiar very hot, ionizing stars which may be (nearly) metal-free (see Kehrig et al. 2015).

Our statistical analysis shows an important degree of non-homogeneity for the T_e[O III] distribution and that the scatter in T_e[O III] can be larger than that in O/H within the observed [O III] λ4363-emitting region (42 arcsec^2 ∼0.3 kpc^2 at the distance of 18.2 Mpc). We find no statistically significant variations in O/H across the 16 × 16 arcsec^2 PMAS-IFU aperture, indicating a global homogeneity of the oxygen abundances in IZw18 over spatial scales of hundreds of parsecs. The representative metallicity of IZw18 derived here, from individual spaxel measurements, is $12 + \log(\mathrm{O/H}) = 7.11 \pm 0.01$ (error-weighted mean value of O/H and its corresponding statistical error). The prevalence of a substantial degree of homogeneity in O/H over the IZw18 galaxy can constrain its chemical history, suggesting an overall enrichment phase previous to the current burst.

We took advantage of our IFU data to create 1D integrated spectra for regions of interest in the galaxy. For the first time, we derive the IZw18 integrated spectrum by summing the spaxels over the whole FOV. Physical–chemical properties of the ionized gas were derived from these selected region spectra. In the three BPT diagrams, all the integrated regions fall within the area corresponding to H II-like ionization. Putting together the spatially resolved measurements and integrated ones of O/H, we find that the IZw18 integrated spectrum-O/H concurs with the representative metallicity of IZw18 defined here, and can be taken to describe the abundance of the ionized gas of IZw18 as a whole. We also show that the derivation of O/H does not depend on the aperture size used. This is a relevant result for studies of high-z SF metal-poor objects for which only the integrated spectra are available.

ACKNOWLEDGEMENTS

We are very grateful to our referee for providing constructive comments and help in improving the manuscript. We wish to thank Martin M. Roth as the PI of the PMAS IFU at the CAHA 3.5 m which allowed us to carry out the first IFS study of the landmark galaxy IZw18. We also thank the CAHA staff for their help during the observations. This work has been partially funded by research projects AYA2010-21887-C04-01 and AYA2013-47742-C04-01 from the Spanish PNAYA, and PEX2011-FQM7058 from Junta de Andalucia. JDHF acknowledges support through the FAPESP grant Project 2012/13381-0.

REFERENCES

Aloisi A. et al., 2007, ApJ, 667, L151
Asplund M., Grevesse N., Sauval A. J., Scott P., 2009, ARA&A, 47, 481
Baggett S. et al., 2002, in HST WFPC2 Data Handbook, V.4.0, edn. B. Mobaster, Baltimore, STScI
Baldwin J. A., Phillips M. M., Terlevich R., 1981, PASP, 93, 5 (BPT)
Blair W. P., Kirshner R. P., Chevalier R. A., 1981, ApJ, 247, 879
Bromm V., 2013, Rep. Progress Phys., 76, 112901
Brown M. J. I. et al., 2014, ApJS, 212, 18
Cairós L. M., Caon N., Zurita C., Kehrig C., Weilbacher P., Roth M., 2009a, A&A, 507, 1291
Cairós L. M., Caon N., Papaderos P., Kehrig C., Weilbacher P., Roth M. M., Zurita C., 2009b, ApJ, 707, 1676
Cairós L. M., Caon N., Zurita C., Kehrig C., Roth M., Weilbacher P., 2010, A&A, 520, A90
Cannon J. M., Skillman E. D., Garnett D. R., Dufour R. J., 2002, ApJ, 565, 931
Cardelli J. A., Clayton G. C., Mathis J. S., 1989, ApJ, 345, 245
Contreras Ramos R. et al., 2011, ApJ, 739, 74
Crowther P. A., 2007, ARA&A, 45, 177
Davidson K., Kinman T. D., Friedman S. D., 1989, AJ, 97, 1591
Diaz A. I., Terlevich E., Pagel B. E. J., Vilchez J. M., Edmunds M. G., 1987, MNRAS, 226, 19
Dopita M. A., Sutherland R. S., 1996, ApJS, 102, 161
Fisher D. B. et al., 2014, Nature, 505, 186
Garnett D. R., Skillman E. D., Dufour R. J., Shields G. A., 1997, ApJ, 481, 174
Gil de Paz A., Madore B. F., Pevunova O., 2003, ApJS, 147, 29
Gomes J. M. et al., 2016, A&A, 588, A68
Heckman T. M., Robert C., Leitherer C., Garnett D. R., van der Rydt F., 1998, ApJ, 503, 646
Hunter D. A., Hoffman L., 1999, AJ, 117, 2789
Hunter D. A., Thronson H. A., Jr, 1995, ApJ, 452, 238
Izotov Y. I., Thuan T. X., 1999, ApJ, 511, 639
Izotov Y. I., Foltz C. B., Green R. F., Guseva N. G., Thuan T. X., 1997, ApJ, 487, L37
Izotov Y. I., Stasińska G., Meynet G., Guseva N. G., Thuan T. X., 2006, A&A, 448, 955
Izotov Y. I., Thuan T. X., Guseva N. G., 2012, A&A, 546, A122
James B. L., Tsamis Y. G., Barlow M. J., 2010, MNRAS, 401, 759
James B. L., Auger M., Aloisi A., Calzetti D., Kewley L., 2016, ApJ, 816, 40
Kauffmann G. et al., 2003, MNRAS, 346, 1055
Kehrig C., Telles E., Cuisinier F., 2004, AJ, 128, 1141
Kehrig C., Vílchez J. M., Telles E., Cuisinier F., Pérez-Montero E., 2006, A&A, 457, 477
Kehrig C., Vílchez J. M., Sánchez S. F., Telles E., Pérez-Montero E., Martín-Gordón D., 2008, A&A, 477, 813
Kehrig C. et al., 2011, A&A, 526, A128
Kehrig C. et al., 2012, A&A, 540, A11
Kehrig C. et al., 2013, MNRAS, 432, 2731
Kehrig C., Vílchez J. M., Pérez-Montero E., Iglesias-Páramo J., Brinchmann J., Kunth D., Durret F., Bayo F. M., 2015, ApJ, 801, L28
Kewley L. J., Dopita M. A., Sutherland R. S., Heisler C. A., Trevena J., 2001, ApJ, 556, 121
Kewley L. J., Dopita M. A., Leitherer C., Davé R., Yuan T., Allen M., Groves B., Sutherland R., 2013, ApJ, 774, 100
Kunth D., Östlin G., 2000, A&AR, 10, 1
Kunth D., Sargent W. L. W., 1986, ApJ, 300, 496
Kunth D., Matteucci F., Marconi G., 1995, A&A, 297, 634
Lebouteiller V., Heap S., Hubeny I., Kunth D., 2013, A&A, 553, A16
Legrand F., Kunth D., Roy J. R., Mas-Hesse J. M., Walsh J. R., 1997, A&A, 326, L17
Legrand F., Kunth D., Roy J.-R., Mas-Hesse J. M., Walsh J. R., 2000, A&A, 355, 891
Leitherer C., Ekström S., Meynet G., Schaerer D., Agienko K. B., Levesque E. M., 2014, ApJS, 212, 14
Lequeux J., Peimbert M., Rayo J. F., Serrano A., Torres-Peimbert S., 1979, A&A, 80, 155
Lilliefors H. W., 1967, J. Am. Stat. Assoc., 62, 399
Luridiana V., Morisset C., Shaw R. A., 2015, A&A, 573, A42
McCall M. L., Rybski P. M., Shields G. A., 1985, ApJS, 57, 1
McGaugh S. S., 1991, ApJ, 380, 140
Melekh B., Recchi S., Hensler G., Buhajenko O., 2015, MNRAS, 450, 111

Mollá M., Vílchez J. M., Gavilán M., Díaz A. I., 2006, MNRAS, 372, 1069
Monreal-Ibero A., Relaño M., Kehrig C., Pérez-Montero E., Vílchez J. M., Kelz A., Roth M. M., Streicher O., 2011, MNRAS, 413, 2242
Nakajima K., Ouchi M., Shimasaku K., Hashimoto T., Ono Y., Lee J. C., 2013, ApJ, 769, 3
O'Halloran B., Madden S. C., Abel N. P., 2008, ApJ, 681, 1205
Osterbrock D. E., Ferland G. J., 2006, Astrophysics of Gaseous Nebulae and Active Galactic Nuclei. University Science Books, CA
Pagel B. E. J., Edmunds M. G., Blackwell D. E., Chun M. S., Smith G., 1979, MNRAS, 189, 95
Pagel B. E. J., Simonson E. A., Terlevich R. J., Edmunds M. G., 1992, MNRAS, 255, 325
Papaderos P., Östlin G., 2012, A&A, 537, A126
Papaderos P. et al., 2013, A&A, 555, LL1
Peimbert M., Sarmiento A., Fierro J., 1991, PASP, 103, 815
Pérez-Montero E., 2014, MNRAS, 441, 2663
Pérez-Montero E., Contini T., 2009, MNRAS, 398, 949
Pérez-Montero E., Díaz A. I., 2005, MNRAS, 361, 1063
Pérez-Montero E., García-Benito R., Díaz A. I., Pérez E., Kehrig C., 2009, A&A, 497, 53
Pérez-Montero E., García-Benito R., Hägele G. F., Díaz Á. I., 2010, MNRAS, 404, 2037
Pérez-Montero E. et al., 2011, A&A, 532, A141
Pérez-Montero E., Kehrig C., Brinchmann J., Vílchez J. M., Kunth D., Durret F., 2013, Adv. Astron., 837, 392
Pilyugin L. S., 2000, A&A, 362, 325
Pilyugin L. S., Vílchez J. M., Thuan T. X., 2006, MNRAS, 370, 1928
Recchi S., Hensler G., 2013, A&A, 551, A41
Recchi S., Matteucci F., D'Ercole A., Tosi M., 2004, A&A, 426, 37
Rola C., Pelat D., 1994, A&A, 287, 676
Roth M. M. et al., 2005, PASP, 117, 620
Roth M. M. et al., 2010, Proc. SPIE, 7742, 774209
Roy J.-R., Kunth D., 1995, A&A, 294, 432
Sánchez S. F. et al., 2015, A&A, 574, A47
Sandin C., Becker T., Roth M. M., Gerssen J., Monreal-Ibero A., Böhm P., Weilbacher P., 2010, A&A, 515, A35
Schaerer D., 2003, A&A, 397, 527
Schlegel D. J., Finkbeiner D. P., Davis M., 1998, ApJ, 500, 525
Searle L., Sargent W. L. W., 1972, ApJ, 173, 25
Skillman E. D., 1985, ApJ, 290, 449
Skillman E. D., Kennicutt R. C., Jr, 1993, ApJ, 411, 655
Thuan T. X., Izotov Y. I., 2005, ApJS, 161, 240
Tumlinson J., Shull J. M., 2000, ApJ, 528, L65
Vaduvescu O., Kehrig C., Bassino L. P., Smith Castelli A. V., Calderón J. P., 2014, A&A, 563, AA118
van Zee L., Westpfahl D., Haynes M. P., Salzer J. J., 1998, AJ, 115, 1000
Vílchez J. M., 1995, AJ, 110, 1090
Vílchez J. M., Iglesias-Páramo J., 1998, ApJ, 508, 248
Vilchez J. M., Pagel B. E. J., 1988, MNRAS, 231, 257
Westera P., Cuisinier F., Telles E., Kehrig C., 2004, A&A, 423, 133
Yin J., Matteucci F., Vladilo G., 2011, A&A, 531, A136
Zwicky F., 1966, ApJ, 143, 192

This paper has been typeset from a TEX/LATEX file prepared by the author.